

Multiplicities of charged pions and kaons from semi-inclusive deep-inelastic scattering by the proton and the deuteron

A. Airapetian,^{13,16} N. Akopov,²⁷ Z. Akopov,⁶ E.C. Aschenauer,^{7,*} W. Augustyniak,²⁶ R. Avakian,²⁷ A. Avetissian,²⁷ E. Avetisyan,⁶ S. Belostotski,¹⁹ H.P. Blok,^{18,25} A. Borissov,⁶ J. Bowles,¹⁴ I. Brodski,¹³ V. Bryzgalov,²⁰ J. Burns,¹⁴ M. Capiluppi,¹⁰ G.P. Capitani,¹¹ E. Cisbani,²² G. Ciullo,¹⁰ M. Contalbrigo,¹⁰ P.F. Dalpiaz,¹⁰ W. Deconinck,⁶ R. De Leo,² L. De Nardo,^{12,6} E. De Sanctis,¹¹ M. Diefenthaler,^{15,9} P. Di Nezza,¹¹ M. Düren,¹³ M. Ehrenfried,¹³ G. Elbakian,²⁷ F. Ellinghaus,⁵ R. Fabbri,⁷ A. Fantoni,¹¹ L. Felawka,²³ S. Frullani,²² D. Gabbert,⁷ G. Gapienko,²⁰ V. Gapienko,²⁰ F. Garibaldi,²² G. Gavrilov,^{6,19,23} V. Gharibyan,²⁷ F. Giordano,^{15,10} S. Gliske,¹⁶ M. Golembiovskaya,⁷ C. Hadjidakis,¹¹ M. Hartig,⁶ D. Hasch,¹¹ A. Hillenbrand,⁷ M. Hoek,¹⁴ Y. Holler,⁶ I. Hristova,⁷ Y. Imazu,²⁴ A. Ivanilov,²⁰ A. Izotov,¹⁹ H.E. Jackson,¹ H.S. Jo,¹² S. Joosten,^{15,12} R. Kaiser,^{14,†} G. Karyan,²⁷ T. Keri,^{14,13} E. Kinney,⁵ A. Kisselev,¹⁹ N. Kobayashi,²⁴ V. Korotkov,²⁰ V. Kozlov,¹⁷ P. Kravchenko,^{9,19} V.G. Krivokhijine,⁸ L. Lagamba,² L. Lapikás,¹⁸ I. Lehmann,¹⁴ P. Lenisa,¹⁰ A. López Ruiz,¹² W. Lorenzon,¹⁶ B.-Q. Ma,³ D. Mahon,¹⁴ B. Maiheu,^{12,‡} N.C.R. Makins,¹⁵ S.I. Manaenkov,¹⁹ L. Manfré,²² Y. Mao,³ B. Marianski,²⁶ A. Martinez de la Ossa,^{6,5} H. Marukyan,²⁷ C.A. Miller,²³ Y. Miyachi,^{24,§} A. Movsisyan,²⁷ M. Murray,¹⁴ A. Mussgiller,^{6,9} E. Nappi,² Y. Naryshkin,¹⁹ A. Nass,⁹ M. Negodaev,⁷ W.-D. Nowak,⁷ L.L. Pappalardo,¹⁰ R. Perez-Benito,¹³ A. Petrosyan,²⁷ M. Raithel,⁹ P.E. Reimer,¹ A.R. Reolon,¹¹ C. Riedl,⁷ K. Rith,⁹ G. Rosner,¹⁴ A. Rostomyan,⁶ J. Rubin,^{1,15} D. Ryckbosch,¹² Y. Salomatin,²⁰ F. Sanftl,²⁴ A. Schäfer,²¹ G. Schnell,^{4,12} B. Seitz,¹⁴ T.-A. Shibata,²⁴ V. Shutov,⁸ M. Stancari,¹⁰ M. Statera,¹⁰ E. Steffens,⁹ J.J.M. Steijger,¹⁸ J. Stewart,⁷ F. Stinzinger,⁹ S. Taroian,²⁷ A. Terkulov,¹⁷ R. Truty,¹⁵ A. Trzcinski,²⁶ M. Tytgat,¹² Y. Van Haarlem,¹² C. Van Hulse,^{4,12} D. Veretennikov,¹⁹ I. Vilardi,² C. Vogel,⁹ S. Wang,³ S. Yaschenko,^{7,9} Z. Ye,⁶ S. Yen,²³ W. Yu,¹³ V. Zagrebelnyy,^{6,13} D. Zeiler,⁹ B. Zihlmann,⁶ and P. Zupranski²⁶

(The HERMES Collaboration)

¹Physics Division, Argonne National Laboratory, Argonne, Illinois 60439-4843, USA

²Istituto Nazionale di Fisica Nucleare, Sezione di Bari, 70124 Bari, Italy

³School of Physics, Peking University, Beijing 100871, China

⁴Department of Theoretical Physics, University of the Basque Country UPV/EHU, 48080 Bilbao, Spain and IKERBASQUE, Basque Foundation for Science, 48011 Bilbao, Spain

⁵Nuclear Physics Laboratory, University of Colorado, Boulder, Colorado 80309-0390, USA

⁶DESY, 22603 Hamburg, Germany

⁷DESY, 15738 Zeuthen, Germany

⁸Joint Institute for Nuclear Research, 141980 Dubna, Russia

⁹Physikalisches Institut, Universität Erlangen-Nürnberg, 91058 Erlangen, Germany

¹⁰Istituto Nazionale di Fisica Nucleare, Sezione di Ferrara and

Dipartimento di Fisica, Università di Ferrara, 44100 Ferrara, Italy

¹¹Istituto Nazionale di Fisica Nucleare, Laboratori Nazionali di Frascati, 00044 Frascati, Italy

¹²Department of Physics and Astronomy, Ghent University, 9000 Gent, Belgium

¹³Physikalisches Institut, Universität Gießen, 35392 Gießen, Germany

¹⁴SUPA, School of Physics and Astronomy, University of Glasgow, Glasgow G12 8QQ, United Kingdom

¹⁵Department of Physics, University of Illinois, Urbana, Illinois 61801-3080, USA

¹⁶Randall Laboratory of Physics, University of Michigan, Ann Arbor, Michigan 48109-1040, USA

¹⁷Lebedev Physical Institute, 117924 Moscow, Russia

¹⁸National Institute for Subatomic Physics (Nikhef), 1009 DB Amsterdam, The Netherlands

¹⁹B. P. Konstantinov Petersburg Nuclear Physics Institute, Gatchina, 188300 Leningrad region, Russia

²⁰Institute for High Energy Physics, Protvino, 142281 Moscow region, Russia

²¹Institut für Theoretische Physik, Universität Regensburg, 93040 Regensburg, Germany

²²Istituto Nazionale di Fisica Nucleare, Sezione di Roma, Gruppo

Collegato Sanità and Istituto Superiore di Sanità, 00161 Roma, Italy

²³TRIUMF, Vancouver, British Columbia V6T 2A3, Canada

²⁴Department of Physics, Tokyo Institute of Technology, Tokyo 152, Japan

²⁵Department of Physics and Astronomy, VU University, 1081 HV Amsterdam, The Netherlands

²⁶National Centre for Nuclear Research, 00-689 Warsaw, Poland

²⁷Yerevan Physics Institute, 375036 Yerevan, Armenia

(Dated: August 5, 2022)

Multiplicities in semi-inclusive deep-inelastic scattering are presented for each charge state of π^\pm and K^\pm mesons. The data were collected by the HERMES experiment at the HERA storage ring using 27.6 GeV electron and positron beams incident on a hydrogen or deuterium gas target. The results are presented as a function of the kinematic quantities x_B , Q^2 , z , and $P_{h\perp}$. They represent

a unique data set for identified hadrons that will significantly enhance our understanding of the fragmentation of quarks into final-state hadrons in deep-inelastic scattering.

I. INTRODUCTION

Isolated quarks have never been observed in nature. When a quark or antiquark is ejected from a bound state of quarks and gluons by absorption of a high-energy photon, as it separates from the ensemble, a shower or "jet" of hadrons is produced. This process may be considered to proceed through the generation of additional quark-antiquark pairs from the color-field, which eventually combine with the original quark or antiquark and with each other until a configuration of color-singlet multi-quark states is reached. Understanding this hadronization process is an essential element of a complete picture of the interaction of quarks in Quantum Chromodynamics (QCD), and is basic to an understanding of the dynamics of quark-quark, gluon-gluon, and quark-gluon interactions. It is described by the polarization-averaged fragmentation function (FF) D_f^h , which is the number density of hadron type h produced by the fragmentation of a struck quark/antiquark of flavor f .

The flavor dependence of fragmentation functions provides a powerful tool for probing the flavor structure of the nucleon in hadron-induced hard scattering and in semi-inclusive deep-inelastic scattering (SIDIS). In the framework of perturbative QCD (pQCD) at leading twist, SIDIS is viewed as the hard scattering of a lepton off a quark or antiquark, which subsequently hadronizes into, e.g., a final-state pion, kaon or proton (or their antiparticles). According to factorization theorems [1, 2], SIDIS can be described in leading-twist pQCD by three components: parton distribution functions (PDFs), hard scattering cross sections, and FFs. The hard scattering cross section is calculable from pQCD. The PDFs parameterize the flavor structure of the initial hadron state. Both the PDFs and the FFs are non-perturbative quantities, but in the collinear framework where they are integrated over parton transverse momentum, they are believed to be universal, i.e., not to depend on the particular type of process from which they were determined [3, 4]. The data available [5] demonstrate that fragmentation of a quark (antiquark) of a specific flavor is favored for a final-state hadron that contains a quark (antiquark) of that flavor as a valence quark (antiquark). The strong flavor correlation is reflected in the magnitude of FFs for "favored" and "unfavored" fragmentation. This correla-

tion is exploited in SIDIS experiments to probe the flavor structure of the nucleon through the technique of flavor tagging, e.g., to extract the flavor dependence of quark-helicity distributions in the proton and deuteron [6]. It can be used to extract quantities of interest such as the flavor asymmetry in the light quark sea from meson yields in SIDIS on the proton and neutron [7, 8].

While the knowledge of PDFs is highly developed, the data available to date for FFs have been much more limited, particularly for unfavored fragmentation. Most extractions of FFs [9–12] rely on high precision information from electron-positron annihilation into charged hadrons, which is available at high energy from experiments at SLAC and LEP (e.g., Refs. [13–16]), and has the advantage of not being convoluted with PDFs. However, these data do not distinguish between quark and antiquark contributions because they are only sensitive to the charge sum of specific hadron species (e.g., $\pi^+ + \pi^-$). In addition, most data are taken at the mass scale of the Z boson, at which electroweak couplings become approximately equal and thus only flavor singlet combinations of FFs can be determined. Also, because all available data is at the same energy scale, determination of the evolution with respect to the four-momentum transfer Q^2 of FFs is difficult. The database has been expanded in recent years with the inclusion of results for inclusive single-hadron production in proton-proton collisions at RHIC. These include measurements of the transverse-momentum spectra of neutral pions at central rapidities at PHENIX [17], and at forward rapidities with STAR [18], as well as similar measurements for identified pions and kaons for forward rapidities at BRAHMS [19].

Accurate measurement of normalized yields of specific hadrons in the final state in SIDIS, i.e., particle multiplicities, provides a means of extracting FFs at much lower energy scales than those of the collider measurements. The HERMES experiment with its highly developed particle identification and pure gas targets is ideally suited for such measurements. The data presented here were extracted from measurements of lepton production of pseudo-scalar mesons in SIDIS that used the 27.6 GeV lepton beam of the HERA storage ring at DESY, which operated with electrons or positrons. The extraction of multiplicities of pions and kaons separately for positive and negative charge provides sensitivity to the individual quark and antiquark flavors in the fragmentation process. The data presented here for proton and deuteron targets are the most precise results for multiplicities currently available at this energy scale. With the inclusion of the kinematic dependence of the multiplicities on the component of hadron momentum transverse to the momentum transfer $P_{h\perp}$, these data reach beyond the standard collinear factorization, and access the transverse-momentum dependence of the fragmentation process. A preliminary version of a subset of these data has already

* Now at: Brookhaven National Laboratory, Upton, New York 11772-5000, USA

† Now at: International Atomic Energy Agency, 1400 Vienna, Austria

‡ Now at: VITO - Flemish Institute for Technological Research, Environmental Modelling Department, 2400 Mol, Belgium

§ Now at: Department of Physics, Yamagata University Yamagata, 990-8560, Japan

been used in a recent FF extraction [20–22]. The data extend those of an earlier HERMES publication [23] that reported results for pion fragmentation on the proton.

This paper is organized in the following way: Sect. II describes the experimental arrangement, while the analysis is detailed in Sect. III. The hadron multiplicities are presented in Sect. IV, and in Sect. V they are compared with leading order (LO) calculations based on recent global fits of FFs. The results are summarized in Sec. VI.

II. THE EXPERIMENT

HERMES was a fixed target experiment which used the lepton beam of the HERA lepton-proton collider at DESY. The lepton ring stored electrons or positrons at an energy of 27.6 GeV. Typical initial beam currents were between 30-50 mA. The HERMES gaseous target [24] was internal to the lepton beam line. It consisted of a 40 cm long open-ended elliptical storage cell aligned coaxially to the beam. The storage cell was made of 75 μm thick Al and could be operated with a variety of atomic gases. This innovative technique allowed the collection of data with little to no dilution from other nuclear material. Part of the data was collected using a polarized target generated by an atomic beam source [25], which could produce a jet of polarized atomic hydrogen or deuterium with an average nuclear polarization around 85% and an areal density of 7.6×10^{13} nucleons/cm² (hydrogen) or 2.1×10^{14} nucleons/cm² (deuterium). The nuclear polarization of the atoms was reversed at 1-3 minute intervals. Unpolarized data were obtained using an unpolarized gas feed system, operating with areal densities of 10^{14} to 10^{17} nucleons/cm². The high density unpolarized target was used only for end-of-fill running where the beam current was much lower than the average for the full fill. The resulting luminosities were of the order of 10^{31} to 10^{33} nucleons/(cm² s). For this analysis, data collected with nuclear-polarized and unpolarized hydrogen and deuterium were used.

The HERMES spectrometer was a forward angle spectrometer with a geometrical acceptance of ± 170 mrad horizontally and $\pm |40 - 140|$ mrad vertically. The HERA beam lines passed through the spectrometer and were shielded in the magnet area by a horizontal iron plate, dividing the spectrometer into two symmetric halves above and below the storage ring plane, thereby limiting the vertical acceptance close to the beam line. The spectrometer consisted of a front and a rear part separated by a 1.5 Tm dipole magnet. Both parts contained tracking devices, while the back part also contained particle identification (PID) detectors. A schematic side view of the spectrometer can be seen in Fig. 1; a detailed description is available in Ref. [26].

Track reconstruction was performed using horizontal-drift chambers before (FC 1/2) [27] and behind (BC 1/2, 3/4) [28] the spectrometer magnet. Combining tracks

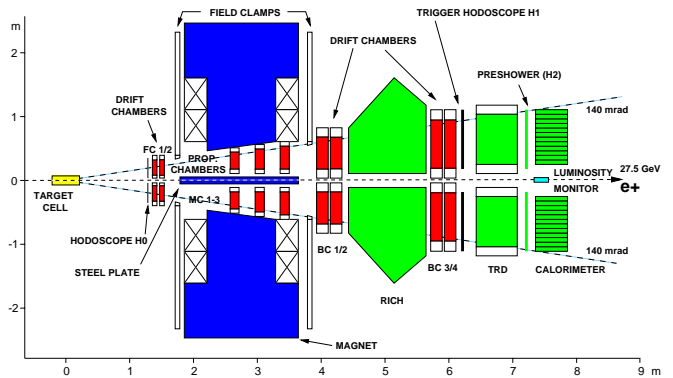


FIG. 1. Schematic view of the HERMES spectrometer.

from the front and back part of the detector allowed the determination of the particle momenta with an intrinsic momentum resolution $\Delta p/p$ between 0.015 and 0.025 in the accessible momentum range.

The tracks found after the spectrometer magnet were also used to identify hits in the PID detectors. Lepton-hadron separation was provided by combining the information of a Ring-Imaging Čerenkov detector (RICH) [29], a preshower detector (H2), a transition-radiation detector (TRD) and a lead-glass calorimeter [30]. More details on the use and the performance of these PID detectors can be found in Ref. [6].

Charged pions, kaons, protons and anti-protons were identified using information from the RICH detector. In order to achieve good separation over a momentum range of 2 to 15 GeV, the RICH made use of two radiators. Particles first traversed a wall of aerogel tiles with index of refraction $n = 1.03$ mounted just behind the entrance window. The second radiator consisted of C_4F_{10} gas ($n = 1.0014$) filling the volume behind the aerogel tiles up to a spherical-mirror array with a radius of curvature of 220 cm. The array deflected the light produced on to a matrix of 1934 photo-multiplier tubes per detector half.

III. DATA ANALYSIS

The analysis was performed on data recorded in the years 2000, 2004 and 2005. Data taken with both polarized and unpolarized targets are included, where the regular switching of the spin direction during polarized running results in effectively unpolarized data when combined. The integrated luminosities for the data sets used in this analysis are shown in Tab. I.

The data were selected using the following criteria:

- There exists a trigger composed of the signals of three hodoscopes (H0, H1, H2) and the electromagnetic calorimeter in coincidence with the HERA lepton-bunch crossing clock.
- Data quality criteria are met, including good per-

Year	Hydrogen (pb ⁻¹)	Deuterium (pb ⁻¹)
2000	132.7	167.0
2004	31.0	24.3
2005	108.2	137.3

TABLE I. Integrated luminosities in pb⁻¹ for the two target gases and the three data taking-years included in this analysis.

formance of the particle identification and tracking detectors, and of the data acquisition system.

- The highest momentum particle identified as lepton originates from the target cell and is within the geometric acceptance of the spectrometer.
- All other charged tracks originate from the target cell and meet the geometric acceptance conditions.

The spectrometer acceptance was limited by the calorimeter dimensions and by the acceptance of the spectrometer magnet. This translates into an acceptance in terms of the polar scattering angle of 40 mrad $\leq \theta \leq$ 220 mrad with respect to the center of the target.

A. Kinematic requirements

The kinematic constraints on events are given by the spectrometer aperture and the requirement that the event kinematics satisfy the conditions $Q^2 > 1 \text{ GeV}^2$ and $W^2 > 10 \text{ GeV}^2$, which select the deep-inelastic scattering (DIS) regime and suppress the region of nucleon resonances, respectively. The relevant kinematic quantities are defined in Table II. The limits on the fractional energy transfer to the target, $0.1 < y < 0.85$, exclude the region where the momentum resolution starts to degrade [26] (lower limit) and the low momentum region (upper limit) where the trigger efficiencies have not yet reached a plateau as a function of momentum. The upper y limit also excludes the kinematic region where large radiative corrections to inclusive cross sections are required.

Hadrons are required to have a momentum of $2 \text{ GeV} < P_h < 15 \text{ GeV}$, given by the operation range of the RICH detector. Data that are not explicitly binned in the fractional hadron energy z also are constrained to $0.2 < z < 0.8$ to exclude the region at high z , which receives a sizeable contribution from exclusive processes, and to suppress the target fragmentation region at low z .

B. Particle identification

Leptons and hadrons are identified based on the combined responses of the TRD, the preshower detector, the

$k = (E, \vec{k}), k' = (E', \vec{k}')$	4-momenta of incident and scattered lepton l'
$P \stackrel{\text{lab}}{=} (M, \vec{0})$	4-momentum of the target nucleon
$q = k - k'$	4-momentum of the virtual photon γ^*
$\nu = \frac{P \cdot q}{M} \stackrel{\text{lab}}{=} E - E'$	Energy transfer to the target
$Q^2 = -q^2 \approx 4EE' \sin^2(\frac{\theta}{2})$	Negative squared four-momentum transfer
$W^2 = (P + q)^2$	Squared invariant mass of the photon-nucleon system
$x_B = \frac{Q^2}{2P \cdot q} \stackrel{\text{lab}}{=} \frac{Q^2}{2M \cdot \nu}$	Bjorken scaling variable
$y = \frac{P \cdot q}{P \cdot k} \stackrel{\text{lab}}{=} \frac{\nu}{E}$	Fractional energy of the virtual photon
ϕ_h	Azimuthal angle between the lepton scattering plane and the hadron production plane
$z = \frac{P \cdot p_h}{P \cdot q} \stackrel{\text{lab}}{=} \frac{E_h}{\nu}$	Fractional energy of hadron h
$P_{h\perp} \stackrel{\text{lab}}{=} \frac{ \vec{q} \times \vec{p}_h }{ q }$	Component of the hadron momentum, p_h , transverse to q

TABLE II. Kinematic variables in semi-inclusive deep-inelastic scattering

calorimeter, and the RICH detector. This response provides lepton-hadron separation with an efficiency larger than 98% for leptons with contaminations $< 1\%$ and 99% for hadrons with a lepton contamination of $< 1\%$. The identification of charged pions and kaons using the RICH detector is based on a direct ray tracing algorithm that deduces the most probable particle types from the event-level hit pattern of Čerenkov photons on the photomultiplier matrix. This algorithm is described in the Appendix of [31].

C. Multiplicities

The multiplicity M_n^h of hadrons of the type h produced off a target n is defined as the respective hadron yield N^h normalized to the DIS yield. It can be expressed in terms of the semi-inclusive cross section $d^5\sigma^h$ and the inclusive DIS cross section $d^2\sigma_{\text{DIS}}$:

$$\begin{aligned}
M_n^h(x_B, Q^2, z, P_{h\perp}) &= \frac{1}{\frac{d^2 N_{\text{DIS}}(x_B, Q^2)}{dx_B dQ^2}} \cdot \int_0^{2\pi} \frac{d^5 N^h(x_B, Q^2, z, P_{h\perp}, \phi_h)}{dx_B dQ^2 dz dP_{h\perp} d\phi_h} d\phi_h \\
&= \frac{1}{\frac{d^2 \sigma_{\text{DIS}}(x_B, Q^2)}{dx_B dQ^2}} \cdot \int_0^{2\pi} \frac{d^5 \sigma^h(x_B, Q^2, z, P_{h\perp}, \phi_h)}{dx_B dQ^2 dz dP_{h\perp} d\phi_h} d\phi_h. \quad (1)
\end{aligned}$$

The Born-level multiplicities, i.e., the multiplicities with no limitations in geometric acceptance and corrected for

radiative effects and detector resolution, are extracted from measured multiplicities binned in 3 dimensions: $(x_B, z, P_{h\perp})$ when the multiplicities as a function of x_B are desired, and $(Q^2, z, P_{h\perp})$ when they are to be given as a function of Q^2 . Due to the strong correlation of x_B and Q^2 in the HERMES data simultaneous binning in these two variables would not have an impact on the extraction. A ϕ_h binning has been omitted because of limited statistical precision. However, a possible impact of the ϕ_h dependence of the unpolarized semi-inclusive cross section and of the acceptance has been accounted for in the systematic uncertainties. The 3-dimensional Born-level multiplicities are extracted using correction and unfolding procedures described later in this section, which take into account charge-symmetric background, trigger efficiencies, exclusive vector meson production, kinematic and geometric acceptance effects, and smearing due to radiative effects. After all corrections and unfolding procedures are applied, the final multidimensional binned data are available, and can be integrated to yield the multiplicities in a one- or two-dimensional binning in the desired variables, e.g., the fractional hadron energy z .

1. Charge-symmetric background

Isolated high-energy leptons from charge-symmetric processes like the π^0 Dalitz decays and photon conversion into e^+e^- pairs can produce a signature indistinguishable from that of DIS events. This background is most significant at low Q^2 and is much stronger for inclusive scattering than for SIDIS. It is taken into account by subtracting from the measured DIS or SIDIS event rate the number of corresponding events for which the leading lepton has a charge opposite to that of the beam particles. The correction to the multiplicities is of the order of 1% for DIS and 2% for SIDIS at low z .

2. RICH unfolding

As described in Sec. III B, the hadron identification is based on the response of the RICH detector. The efficiency of the detector is encoded in 3×4 matrices binned in momentum, charge, and event topology (number of tracks in one detector half). They relate the vector of true hadron type T_h with the vector of identified hadron type I_h :

$$\begin{pmatrix} I_\pi \\ I_K \\ I_P \\ I_X \end{pmatrix} = \begin{pmatrix} P_\pi^\pi & P_K^\pi & P_P^\pi \\ P_\pi^K & P_K^K & P_P^K \\ P_\pi^P & P_K^P & P_P^P \\ P_\pi^X & P_K^X & P_P^X \end{pmatrix} \cdot \begin{pmatrix} T_\pi \\ T_K \\ T_P \end{pmatrix}. \quad (2)$$

Here, P_t^i is the probability that a hadron of true type t is identified as hadron of type i . The superscript X refers to unidentified hadrons. The matrices are extracted from a Monte Carlo simulation of the detector response that uses

the PID algorithm. Truncating the X row and inverting the matrix yields a relation that gives a weight, the corresponding element of P_{trunc}^{-1} , with which each identified hadron is counted as pion, kaon or proton:

$$\vec{T} = P_{\text{trunc}}^{-1} \cdot \vec{I}. \quad (3)$$

The uncertainties due to RICH unfolding were estimated to be less than 0.5% for pions and less than 1.5% for kaons.

3. Trigger efficiencies

The required trigger combines information from three hodoscopes and the electromagnetic calorimeter. The efficiencies of the individual detectors are extracted using special calibration triggers, yielding an overall efficiency depending on the track momentum and the event topology (e.g., events with one or two tracks) that ranged from 95% to 99%. The events are weighted with the inverted efficiency factor.

4. Exclusive vector-meson contribution

Exclusive production of vector mesons (ρ^0 , ω , or ϕ) can be described in the Vector Meson Dominance (VMD) model as the fluctuation of the virtual photon into a $q\bar{q}$ -pair before its interaction with the target nucleon. These vector mesons subsequently decay into lighter hadrons that are then found in the final hadronic state. The cross sections for the exclusive production show a $1/Q^6$ dependence and can be considered as higher-twist effects. They do not involve the fragmentation of quarks originating from the target nucleon. If fragmentation functions were to be extracted from multiplicities that include such an exclusive production, they would be process dependent. For this reason the data presented in this paper have been corrected for hadrons stemming from these processes, but the final tabulation includes data with and without this correction.

The fraction of final-state hadrons originating from exclusive vector-meson decay was evaluated in each kinematic bin using the PYTHIA Monte Carlo generator. This PYTHIA version incorporated a VMD model tuned to describe exclusive ρ^0 production at HERMES [32]. Since PYTHIA can only simulate proton or neutron targets, the values for deuterium were constructed as the combination of the values for these nucleons. The major contribution due to exclusive vector mesons to the final state hadron sample arises in the form of pions originating from ρ^0 decay. Due to its anisotropic decay-angle distribution, pions from ρ^0 decay are concentrated at low and high z . For the low statistics high z region near $z = 1$, it is estimated that up to 50% of the charged pions originate from ρ^0 , while at low z this fraction is negligible due to the much larger yield from other channels. For kaons, the contribution from ϕ decay is less than

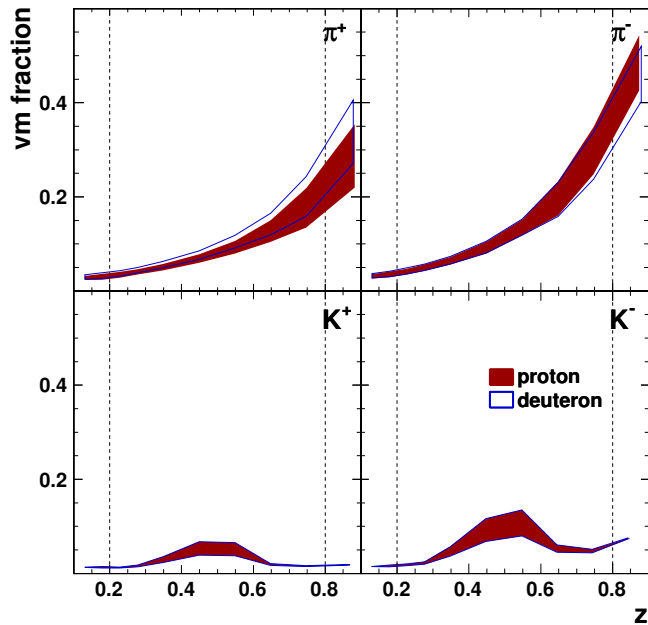


FIG. 2. Fraction of mesons generated by the decay of exclusive vector mesons as a function of z , from PYTHIA (see text). The widths of the bands indicate the uncertainty in the corresponding fractions. The vertical dashed lines are the limits in z used in the multiplicity extractions.

10%. Both the SIDIS and the DIS yields which determine the multiplicities are corrected bin by bin for exclusive vector meson production. The correction for SIDIS is presented in its z projection in Fig. 2. The corresponding integrated correction for DIS is 0.041 for the proton target and 0.044 for the deuteron target. The bands in Fig. 2 for pions describe the range in the correction which correspond to a 1σ variation in the parameterization of the exclusive ρ cross section. For the ϕ meson, the bands are half of the total variation in the correction that results from varying the parameterization of the exclusive ϕ cross section over its total range of uncertainty.

5. Acceptance and radiative effects

Other effects that influence the extracted multiplicities are

- QED radiative effects, such as vertex corrections and the initial and final state radiation of real photons by the incoming or outgoing lepton, that alter the hard scattering amplitude and can mask the true kinematics at the $l\gamma^*$ vertex,
- the limited geometric and kinematic acceptance of the HERMES spectrometer,
- the detector resolution.

These effects were evaluated using two Monte Carlo simulations that use the same LEPTO/JETSET [33, 34] event generator. The first simulation included QED radiative effects and a full detector simulation. Radiative processes and vertex corrections were simulated using the RADGEN generator [35]. The leptons and hadrons produced were tracked through a GEANT3 [36] model of the HERMES spectrometer. Tracks were reconstructed using the same algorithm [26] used for real data.

As this Monte Carlo simulation contains both the generated and reconstructed properties of any recorded track, bin to bin migration of hadron h can be quantified in a migration matrix $n^h(i, j)$, where i ($= 1 \dots s$) refers to the bin number based on reconstructed properties and j ($= 0 \dots s$) to the bin number based on the generated (Born) properties. The additional Born index $j = 0$ refers to background events generated outside the acceptance that migrate into it. The probabilistic information can be summarized in a smearing matrix

$$S^h(i, j) = \frac{n^h(i, j)}{n_{\text{Born}}^h(j)}. \quad (4)$$

The vector $n_{\text{Born}}^h(j)$ is obtained from the second Monte Carlo simulation, generated without radiative or instrumental effects.

As an example, the SIDIS yield of events without radiative or instrumental effects, i.e., the Born yield, Y_{Born}^h is related to the measured SIDIS yield Y_{meas}^h via

$$Y_{\text{Born}}^h(j) = \sum_i [S'^h]^{-1}(j, i) [Y_{\text{meas}}^h(i)R - n^h(i, 0)]. \quad (5)$$

Here $R = \sum_l n_{\text{tracked}}^{\text{DIS}}(l) / \sum_l Y_{\text{meas}}^{\text{DIS}}(l)$ where $n_{\text{tracked}}^{\text{DIS}}(l)$ is the number of inclusive DIS events in bin l in the MC simulation with radiative and instrumental effects and $Y_{\text{meas}}^{\text{DIS}}(i)$ is the measured number of DIS events in bin i . The matrix $[S'^h]^{-1}(j, i)$ is the inverted SIDIS smearing matrix with $j > 0$. Because the Born multiplicity is $Y_{\text{Born}}^h / Y_{\text{Born}}^{\text{DIS}}$, in terms of measured quantities it is given by

$$M_{\text{Born}}^h(j) = \frac{Y_{\text{Born}}^h(j)}{Y_{\text{Born}}^{\text{DIS}}(j)} = \frac{\sum_i [S'^h]^{-1}(j, i) [Y_{\text{meas}}^h(i)R - n^h(i, 0)]}{\sum_k [S'^{\text{DIS}}]^{-1}(j, k) [Y_{\text{meas}}^{\text{DIS}}(k)R - n^{\text{DIS}}(k, 0)]}. \quad (6)$$

If the kinematic binning were *fully differential* in all kinematic variables, in the limit of infinitely small bins the smearing matrix defined by Eq. 4 would be independent of the model embodied in the Monte Carlo event generator for $j > 0$. If the smearing correction were applied after yields were integrated over some kinematic variable(s) on which both the SIDIS yields and the spectrometer acceptance may depend, the accuracy with which the smearing matrix corrects for acceptance effects

would depend on the success of the model in describing this yield dependence. Hence even for those results presented here as a function of only one kinematic variable, this correction is applied using kinematic binning in three dimensions, which is defined in Tabs. III to VI.

D. Systematic uncertainties

1. RICH unfolding

The unfolding algorithm for correcting for the inefficiencies of the RICH detector is based on probability matrices as described in Sec. III C 2. These probability matrices are obtained from a Monte Carlo simulation of the RICH detector, which produces events that are analysed with the same particle identification algorithm (described in the Appendix of [31]) as that used to analyse experimental data. The algorithm is sensitive to the number and distribution of background hits on the photomultiplier matrix. Different background scenarios result in a set of slightly different probability matrices. The variation of the final result when using the different P matrices has been assigned as systematic uncertainty. The most sensitive region is at low momentum (2-4 GeV). Due to their lower relative flux, the uncertainty in the fraction of identified kaons generated by other misidentified hadrons is much larger than that for pions. For the multiplicities presented as a function of z , this contribution to the systematic uncertainty is typically less than 0.5% for pions and 1.5% for kaons.

2. Azimuthal asymmetries in the unpolarized cross section

The unpolarized cross section contains two terms generating a $\cos(\phi_h)$ and $\cos(2\phi_h)$ modulation in the azimuthal angle ϕ_h . These two terms arise, in part, from asymmetries generated by the Cahn [37–40] and the Boer-Mulders [41, 42] effects. The moments of these modulations have been extracted at HERMES [43]. The effect of these modulations is not included in the Monte Carlo simulation used for acceptance corrections. The simulation assumes an azimuthally uniform PYTHIA6 production at the Born level. In order to study the influence of these moments, a second extraction was carried out using a simulation in which the events generated at the Born level are reweighted by means of a 4-dimensional parameterization of the cosine modulations extracted from HERMES data. The difference between the results for the extractions with the original and the reweighted simulations was taken as the systematic uncertainty arising from the effects of azimuthal asymmetries in the unpolarized cross section. For most x_B bins it is less than 2%.

3. Year dependence

Both the proton and deuteron data samples are combinations of data taken over three different years. Comparing the results from the individual years led to differences larger than expected from statistical fluctuations, which could not be assigned to specific sources, but must be attributed to a combination of differences in the data taking conditions (e.g., running with polarized/unpolarized targets). The differences are mainly concentrated in the low momentum region. The largest deviation in the multiplicities between any individual data taking period and the overall result has been taken as a systematic uncertainty. With the exception of a few bins, it is never larger than 2% of the measured value.

4. Finite bin width

The unfolding algorithm which corrects for acceptance, limited detector resolution and radiative effects is independent of the Monte Carlo model used to extract the smearing matrix if the kinematic bins are fully differential and of vanishing width. For this case the effects of imperfections in the model on which the SIDIS Monte Carlo is based are negligible. The potential impact of any residual model dependence due to the finite bin width is estimated by scanning over the JETSET parameters which control the Monte Carlo event generator [44]. This scan is carried out in the space in χ^2 of the fit to measured multiplicities. Nine parameters which constrain various features of the fragmentation process are varied in the scan. An eigenvector basis approach to the Hessian method [45] is used to generate nine-parameter vectors which are uncorrelated orthogonal combinations of the input parameters to the scan. The intersections of these eigenvectors with the χ^2 contour which lies 68% above the best-fit minimum in the scan space, provides input parameter sets that characterize the corresponding uncertainties in the multiplicities arising from those in the JETSET model parameters. The largest deviation of the multiplicities from the values extracted with the standard version of the Monte Carlo is taken as a systematic uncertainty. This uncertainty does not exceed 3-4%.

IV. HADRON MULTIPLICITIES

The Born multiplicities, after correction for exclusive-vector-meson production, are presented in Figs. 3 and 7. In Fig. 3 they are shown for both proton and deuteron targets as a function of the energy fraction z in four panels corresponding to the type of final-state hadron. The individual panels compare data for a given hadron type taken with a hydrogen (full circles) or deuterium (empty squares) target. Error bars on the points for the statistical uncertainties are too small to be visible. The systematic uncertainties are given by the error bands. The

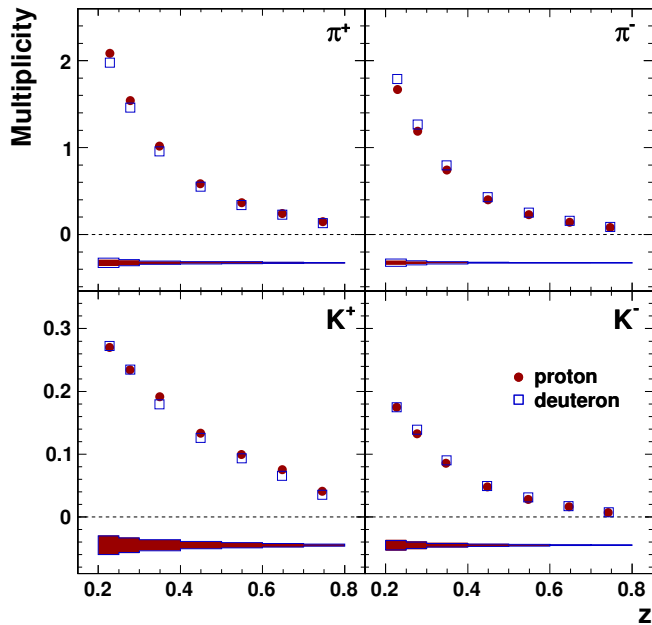


FIG. 3. Multiplicities corrected for exclusive vector mesons as a function of z from a hydrogen target (full circles) and a deuterium target (empty squares). Error bars for the statistical uncertainties are too small to be visible. The systematic uncertainties are given by the error bands.

x_B	0.023 - 0.085 - 0.6
z	0.1 - 0.15 - 0.2 - 0.25 - 0.3 - 0.4 - 0.5 - 0.6 - 0.7 - 0.8 - 1.1
$P_{h\perp}$ (GeV)	0.0 - 0.1 - 0.3 - 0.45 - 0.6 - 1.2

TABLE III. 3D binning used for the unfolding correction of those multiplicities presented as a function of z (Figs. 3 and 5).

z bins are defined in Tab. III (z), which together with Tabs. IV ($P_{h\perp}$), V (x_B) and VI (Q^2) tabulate the binning used in the subsequent multi-dimensional representation of the multiplicities presented in Fig. 7. To indicate the importance of the correction for exclusive vector meson decay, the multiplicities for a proton target of pions and kaons versus z with the fraction of mesons coming from all processes involving exclusive vector meson decay included (open circles) or subtracted (closed circles) are compared in Fig. 4.

The results shown in Fig. 3 for pions (top row) from a proton target are in good agreement with HERMES data published earlier [23]. The proton π^+ multiplicities are slightly larger than those of the deuteron, while for π^- the reverse is true. The ratio of π^+ to π^- for the proton (deuteron) ranges from 1.2 (1.1) in the first z bin to 2.6 (1.8) in the last z bin. These results can be attributed to the dominance of scattering off the u quarks, reflecting the fact that the fragmentation process $u \rightarrow \pi^+$ is

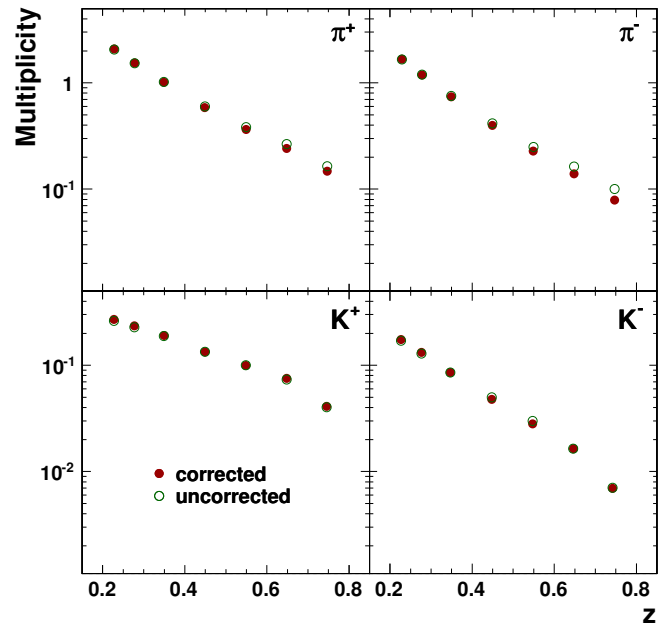


FIG. 4. Comparison of measured Born multiplicities for a proton target with and without the correction for exclusive vector mesons as a function of z . The open (closed) circles include (exclude) exclusive vector meson production. The statistical error bars are too small to be visible.

favoured, while the process $u \rightarrow \pi^-$ is unfavored. With rising z , this effect is enhanced. Similarly, the higher π^- multiplicities for the deuteron are a result of the increased fraction of d quarks in the target and of the stronger favored fragmentation to the π^- from the neutron. The K^+ multiplicity for the proton is slightly larger than for the deuteron, while within errors for K^- the multiplicities are equal. The ratio K^+/K^- rises from 1.5 to 5.7 (proton target) and from 1.3 to 4.6 (deuteron target) for $0.2 < z < 0.8$, reflecting the fact that K^- cannot be produced through favored fragmentation from the nucleon valence quarks.

Fig. 5 shows the asymmetry

$$A_{d-p}^h = \frac{M_{\text{deuteron}}^h - M_{\text{proton}}^h}{M_{\text{deuteron}}^h + M_{\text{proton}}^h} \quad (7)$$

between the hadron production off a proton target and a deuteron target. Because of the near equality of the proton and neutron multiplicities (see Fig. 3), the magnitude of this asymmetry is small, but it reflects details of the quark structure of the targets. The negative values for π^+ and the positive values for π^- reflect the different valence quark content of the target nuclei. The measured asymmetry in Fig. 5 is more pronounced in the high z region for kaons. For positive kaons it is similar to that of π^+ , while the corresponding asymmetry for negative kaons is near zero, except at higher z , suggesting that negative kaons are less sensitive to the valence quark content of the target. A LO calculation (see Sect. V) of

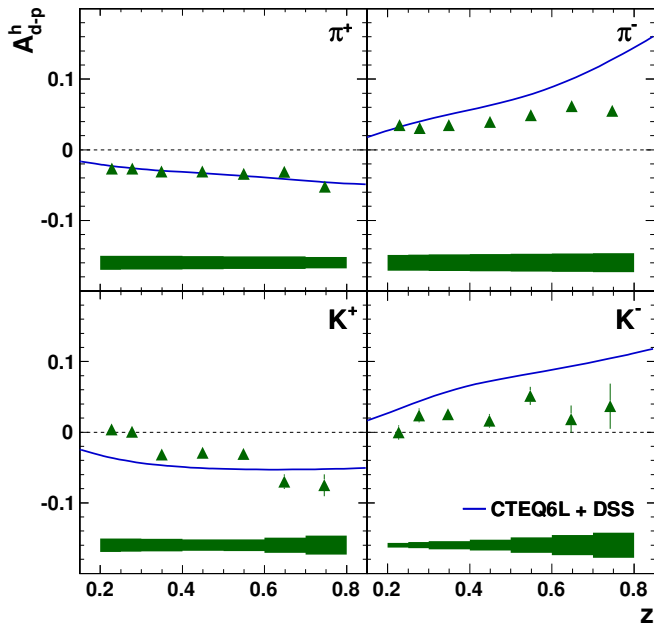


FIG. 5. The asymmetry A_{d-p}^h as defined in Eq. 7 as a function of z , for the multiplicities shown in Fig. 3. The values given by a LO calculation using fragmentation functions from DSS Ref. [22] and parton distributions from CTEQ6L [46] are given by the solid curves.

A_{d-p}^h shown in Fig. 5 reproduces the measured values for positive charge, but strongly overpredicts the asymmetries for negative charge. The same trend of negative values for π^+ and the positive values for π^- is evident in Fig. 6 where the asymmetry A_{d-p}^π is plotted as a function of x_B for four slices in z . There is no strong dependence of A_{d-p}^π on the slice in z or on x_B .

When the statistical precision permits, binning of extracted multiplicities in two or more dimensions can provide useful insights into the correlations between kinematic variables and allow the separation of the effects of PDFs and FFs. In Fig. 7 the multiplicities are presented for positively and negatively charged pions and kaons as a function of transverse hadron momentum $P_{h\perp}$, x_B , and Q^2 for the four slices of z between 0.2 and 0.8. The features of the $P_{h\perp}$ distributions result from the combined effects of the initial transverse motion of the struck quark in SIDIS, of its emission of soft gluon radiation, and of the component of transverse momentum which is generated by the fragmentation process. The multiplicities measured at HERMES as a function of $P_{h\perp}$ peak at increasing $P_{h\perp}$ as z is increased. For negative kaons the distribution versus $P_{h\perp}$ is wider than for positive kaons and may indicate a more extended fragmentation process. In the LUND model [47], which is also used in the HERMES Monte Carlo, fragmentation is modeled by string fragmentation in which the color field between the quarks is the fragmenting entity. That field is modeled as a string with a potential energy that increases with

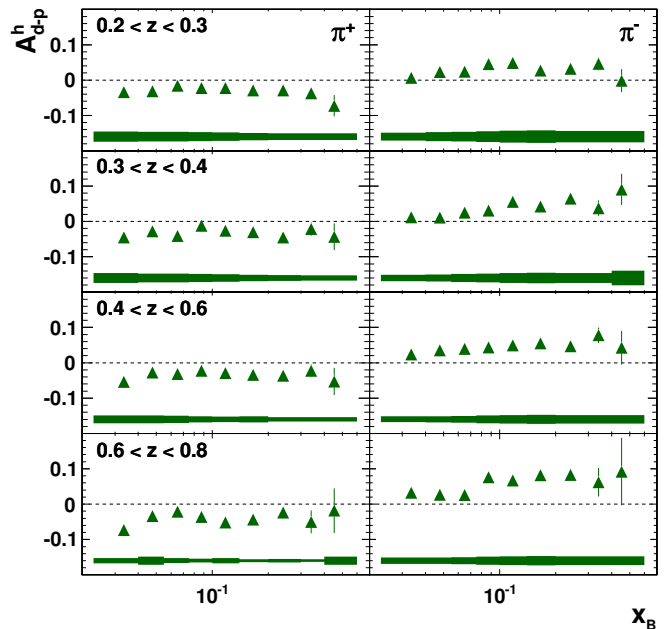


FIG. 6. The asymmetry A_{d-p}^h as defined in Eq. 7 as a function of x_B , for the pion multiplicities shown in Fig. 7. The statistical uncertainty is shown by the error bars, while the systematic uncertainty is given by the error bands.

x_B	0.023 - 0.085 - 0.6
z	0.1 - 0.2 - 0.3 - 0.4 - 0.6 - 0.8 - 1.1
$P_{h\perp}$ (GeV)	0.0 - 0.1 - 0.2 - 0.3 - 0.4 - 0.5 - 0.6 - 0.7 - 0.8 - 1.2

TABLE IV. 3D binning used for the unfolding correction of those multiplicities presented as a function of $P_{h\perp}$ and z (Fig. 7).

increasing quark separation. When the separation is sufficiently large the string breaks. At each string break new quark-antiquark pairs are generated. This typically leads to more string breaks for unfavored fragmentation, which is expected to be more relevant for negative kaons.

In the context of the multiplicity for π^+ and π^- being shown as a function of x_B , it should be noted that at HERMES kinematics there is a strong correlation between x_B and Q^2 . For the binning given in Tab. V, the average value of Q^2 rises from 1 (GeV)² in the lowest x_B

x_B	0.023 - 0.04 - 0.055 - 0.075 - 0.1 - 0.14 - 0.2 - 0.3 - 0.4 - 0.6
z	0.1 - 0.2 - 0.3 - 0.4 - 0.6 - 0.8 - 1.1
$P_{h\perp}$ (GeV)	0.0 - 0.3 - 0.5 - 0.7 - 1.2

TABLE V. 3D binning used for the unfolding correction of those multiplicities presented as a function of x_B and z (Figs. 6 and 7).

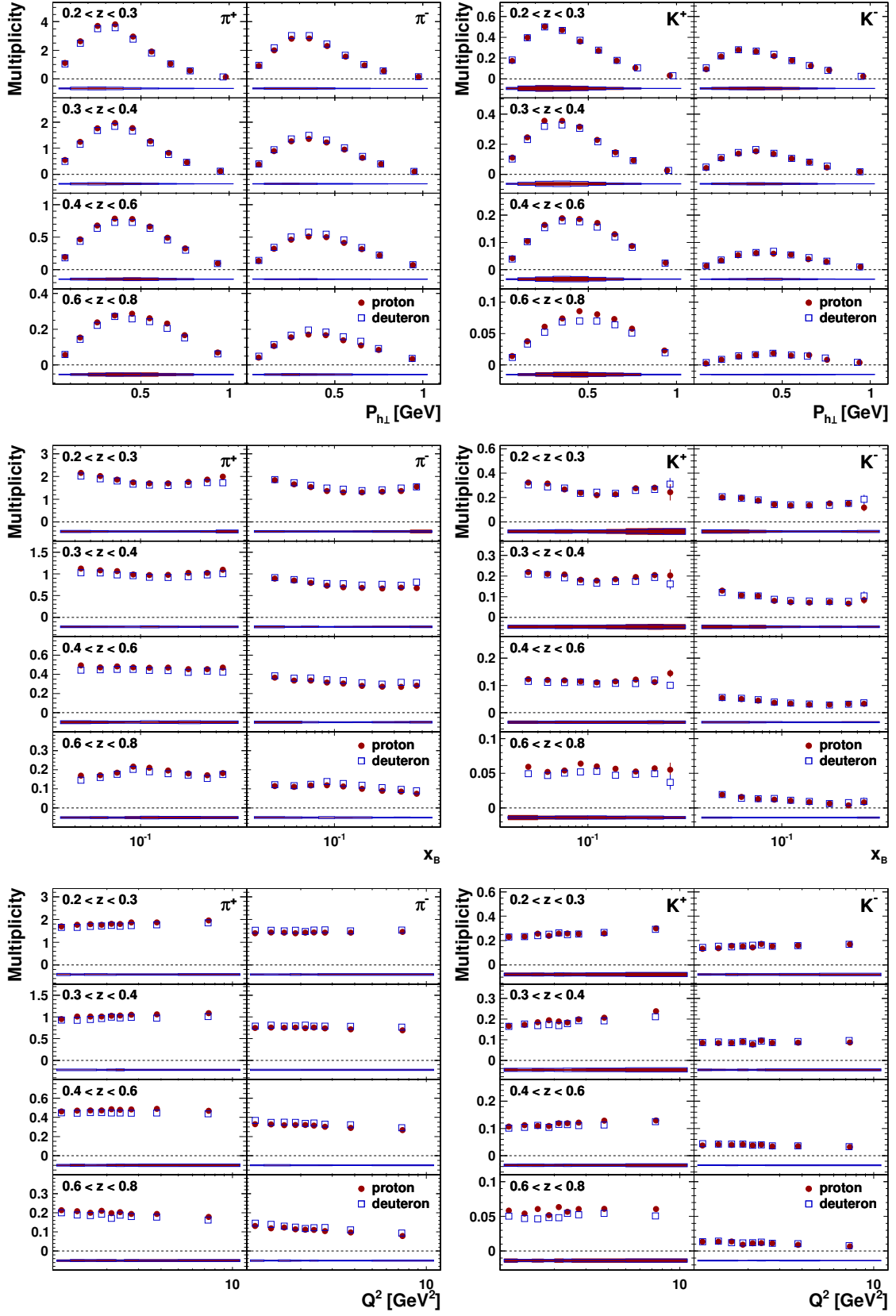


FIG. 7. Multiplicities of pions (left panels) and kaons (right panels) for the proton and the deuteron as a function of $P_{h\perp}$, x_B , and Q^2 in four z bins. Positive charge is on the left and negative charge is on the right of each panel. Uncertainties are as in Fig. 3.

Q^2 (GeV 2)	1. - 1.25 - 1.5 - 1.75 - 2.0 - 2.25 - 2.5 - 3.0 - 5.0 - 15.0
z	0.1 - 0.2 - 0.3 - 0.4 - 0.6 - 0.8 - 1.1
$P_{h\perp}$ (GeV)	0.0 - 0.3 - 0.5 - 0.7 - 1.2

TABLE VI. 3D binning used for the unfolding correction of those multiplicities presented as a function of Q^2 and z (Fig. 7).

bin to 10 (GeV) 2 in the highest bin. A prominent feature of the multiplicity data is their kinematic dependence on x_B , z , and Q^2 . These data are measured at a much lower energy scale than those of most measurements of fragmentation yields. Nevertheless, the same qualitative trends observed at higher scales are present in the data. A strong dependence of the multiplicities on z and a weak or vanishing variation with x_B and Q^2 confirm the continuing applicability of the standard collinear factorization and the universality of distribution and fragmentation functions in the SIDIS cross section at the low scales of HERMES, $\langle Q^2 \rangle = 2.5$ GeV 2 and $W^2 \approx 10$ GeV 2 .

A tabulation of the data is presented [48] in four 3-dimensional decompositions corresponding to the binnings given in Tabs. III (z), IV ($P_{h\perp}$), V (x_B), and VI (Q^2). Because of the unfolding procedure used to extract the Born multiplicities from the measured values, the data in the various kinematic bins are statistically correlated. In using the data tabulated, the accompanying covariance matrix must be considered to insure that statistical uncertainties are not overestimated. In addition, the results of each of the projections of these data discussed in the paper are presented. This complete data base has been generated including both multiplicities which have been corrected for exclusive vector meson production, as presented in this paper, and uncorrected multiplicities.

An earlier extraction [7] of kaon multiplicities, used in an evaluation of the distribution of strange quarks in the nucleon, will be superseded by data extracted using the new multiplicities presented here. In particular, the previous extraction was accomplished using one-dimensional unfolding and multiplicities were presented for hadron momenta larger than 2 GeV. A reevaluation of the strange quark distribution using the newly obtained more accurate kaon data will be presented in a separate forthcoming paper.

V. COMPARISON OF MULTIPLICITIES WITH LO CALCULATIONS

To date, analyses of FFs [9–12] have been carried out in the framework of collinear factorization. In this approximation, the multiplicity is defined as the integration of Eq. 1 over $P_{h\perp}$. In one such model, the LO QCD-improved quark-parton model, the hadron multiplicity as

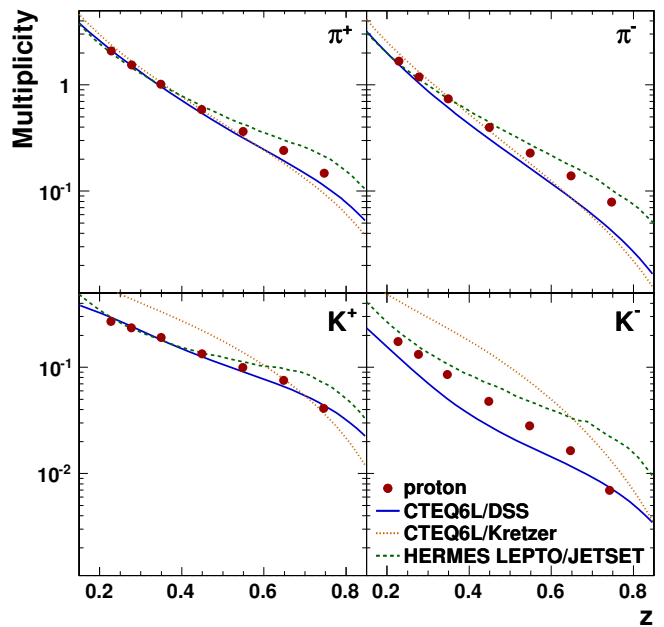


FIG. 8. Comparison of the vector-meson-corrected multiplicities measured for various hadrons with LO calculations using CTEQ6L parton distributions and two compilations (see text) of fragmentation functions. Also shown are the values obtained from the HERMES Lund Monte Carlo. The statistical error bars on the experimental points are too small to be visible.

a function of z and Q^2 is given by

$$\frac{1}{N_{DIS}(Q^2)} \frac{dN^h(z, Q^2)}{dz} = \frac{\sum_f e_f^2 \int_0^1 q_f(x_B, Q^2) dx_B D_f^h(z, Q^2)}{\sum_f e_f^2 \int_0^1 q_f(x_B, Q^2) dx_B}, \quad (8)$$

where the sum is over quarks and antiquarks of flavor f , and e_f is the quark charge in units of the elementary charge. The multiplicities in this LO approximation are a reasonable starting point for comparing the HERMES results with predictions based on fragmentation functions resulting from global QCD analyses of all relevant data.

A comparison of the multiplicities measured by HERMES for SIDIS on the proton with LO predictions is presented in Fig. 8. The multiplicities are calculated from Eq. 8 (though integrated only over the accepted range in x_B of 0.023 to 0.600) using values for the FFs taken from two widely used analyses, that of de Florian *et al.* (DSS) [22] and that of Kretzer [9], together with parton distributions taken from CTEQ6L. For positively charged pions and kaons, the results using FFs from the analysis of DSS are in reasonable agreement with the HERMES results. For negative charges, the discrepancies between data and the results based on FFs from DSS are substantial, particularly for K^- where the curve predicted lies below the observed multiplicity over most of the measured range of z . For π^- the results from the DSS analysis agree with measurement at low z . For both π^- and K^- , fragmentation is less affected by u-quark dominance. Uncertainties in the less abundant production by strange

and anti-u quarks may have a larger impact on the predictions than for the positively charged hadrons. Alternatively, next-to-leading-order (NLO) processes may be proportionally more important for π^- and particularly K^- , and the discrepancies observed here may signal the importance of calculating multiplicities at NLO. For kaons the DSS results give a better representation of the data than the Kretzer curves. This is to be expected, since the DSS analysis included a preliminary version of the HERMES proton data in its database. The Kretzer results are in substantial disagreement with the multiplicities measured for K^- . In Fig. 8 the multiplicities obtained from the HERMES Lund Monte Carlo, in which the fragmentation parameters have been tuned for HERMES kinematic conditions [20] are also shown. Inclusion of the data reported here in future global analyses should result in higher precision in the extraction of FFs, particularly those describing less abundant fragmentation processes.

VI. SUMMARY

HERMES has measured the multiplicity of charge-separated pions and kaons as a function of z , $P_{h\perp}$, x_B and Q^2 produced by SIDIS off a hydrogen and a deuterium target. This high statistics data set, which result from scattering by pure gas targets of protons and deuterons, provides unique information on the fragmentation of quarks into final state hadrons and will contribute valuable input for the extraction of fragmentation functions using QCD fits. The comparison of the results from the two targets supports the notion of fragmentation into hadrons containing the struck quark as valence quark being favored, and will allow more reliable extrac-

tion of unfavored fragmentation functions. The multiplicities measured as a function of $P_{h\perp}$ will provide constraints on models of the motion of quarks in the nucleon in the transverse plane of momentum space, as well as on the models of the fragmentation process.

ACKNOWLEDGEMENTS

We gratefully acknowledge the DESY management for its support and the staff at DESY and the collaborating institutions for their significant effort. This work was supported by the Ministry of Economy and the Ministry of Education and Science of Armenia; the FWO-Flanders and IWT, Belgium; the Natural Sciences and Engineering Research Council of Canada; the National Natural Science Foundation of China; the Alexander von Humboldt Stiftung, the German Bundesministerium für Bildung und Forschung (BMBF), and the Deutsche Forschungsgemeinschaft (DFG); the Italian Istituto Nazionale di Fisica Nucleare (INFN); the MEXT, JSPS, and G-COE of Japan; the Dutch Foundation for Fundamenteel Onderzoek der Materie (FOM); the Russian Academy of Science and the Russian Federal Agency for Science and Innovations; the Basque Foundation for Science (IKERBASQUE) and the UPV/EHU under program UFI 11/55; the U.K. Engineering and Physical Sciences Research Council, the Science and Technology Facilities Council, and the Scottish Universities Physics Alliance; the U.S. Department of Energy (DOE) and the National Science Foundation (NSF); as well as the European Community Research Infrastructure Integrating Activity under the FP7 "Study of strongly interacting matter (HadronPhysics2, Grant Agreement number 227431)".

-
- [1] J. C. Collins, L. Frankfurt, and M. Strikman, *Phys. Rev.* **D56**, 2982 (1997).
 - [2] X. Ji, J.-P. Ma, and F. Yuan, *Phys. Lett.* **B597**, 299 (2004).
 - [3] B. A. Kniehl, G. Kramer, and B. Pötter, *Nucl. Phys.* **B597**, 337 (2001).
 - [4] S. Albino, B. A. Kniehl, G. Kramer, and C. Sandoval, *Phys. Rev.* **D75**, 034018 (2007).
 - [5] F. Arleo, *Eur. Phys. J.* **C61**, 603 (2009).
 - [6] A. Airapetian *et al.* (HERMES Collaboration), *Phys. Rev.* **D71**, 012003 (2005).
 - [7] A. Airapetian *et al.* (HERMES Collaboration), *Phys. Lett.* **B666**, 446 (2008).
 - [8] K. Ackerstaff *et al.* (HERMES Collaboration), *Phys. Rev. Lett.* **81**, 5519 (1998).
 - [9] S. Kretzer, *Phys. Rev.* **D62**, 054001 (2000).
 - [10] B. A. Kniehl, G. Kramer, and B. Pötter, *Nucl. Phys.* **B582**, 514 (2000).
 - [11] S. Albino, B. A. Kniehl, and G. Kramer, *Nucl. Phys.* **B725**, 181 (2005).
 - [12] M. Hirai, S. Kumano, T.-H. Nagai, and K. Sudoh, *Phys. Rev.* **D75**, 094009 (2007).
 - [13] D. Buskulic *et al.*, *Z. Phys.* **C66**, 355 (1995).
 - [14] K. Abe *et al.*, *Phys. Rev.* **D59**, 052001 (1999).
 - [15] P. Abreu *et al.*, *Eur. Phys. J.* **C5**, 585 (1998).
 - [16] G. Abbiendi *et al.* (OPAL Collaboration), *Eur. Phys. J.* **C16**, 407 (2000).
 - [17] S. S. Adler *et al.* (PHENIX Collaboration), *Phys. Rev. Lett.* **91**, 241803 (2003).
 - [18] J. Adams *et al.* (STAR Collaboration), *Phys. Rev. Lett.* **97**, 152302 (2006).
 - [19] I. Arsene *et al.* (BRAHMS Collaboration), *Phys. Rev. Lett.* **98**, 252001 (2007).
 - [20] A. Hillenbrand, *Ph.D. thesis*, Friedrich-Alexander-Universität Erlangen-Nürnberg (2005), DESY-THESIS-2005-035.
 - [21] B. Maiheu, *Ph.D. thesis*, Universiteit Gent (2006).
 - [22] D. de Florian, R. Sassot, and M. Stratmann, *Phys. Rev.* **D75**, 114010 (2007).
 - [23] A. Airapetian *et al.* (HERMES Collaboration), *Eur. Phys. J.* **C21**, 599 (2001).

- [24] A. Airapetian *et al.* (HERMES Collaboration), *Nucl. Instrum. Meth.* **A540**, 68 (2005).
- [25] A. Nass *et al.*, *Nucl. Instrum. Meth.* **A505**, 633 (2003).
- [26] K. Ackerstaff *et al.* (HERMES Collaboration), *Nucl. Instrum. Meth.* **A417**, 230 (1998).
- [27] J. T. Brack *et al.*, *Nucl. Instrum. Meth.* **A469**, 47 (2001).
- [28] S. Bernreuther *et al.*, *Nucl. Instrum. Meth.* **A416**, 45 (1998).
- [29] N. Akopov *et al.*, *Nucl. Instrum. Meth.* **A479**, 511 (2002).
- [30] H. Avakian *et al.*, *Nucl. Instrum. Meth.* **A417**, 69 (1998).
- [31] A. Airapetian *et al.* (HERMES Collaboration), (2012), [arXiv:1204.4161 \[hep-ex\]](https://arxiv.org/abs/1204.4161).
- [32] P. Liebing, *Ph.D. thesis*, Universität Hamburg (2004), DESY-THESIS-2004-036.
- [33] G. Ingelman, A. Edin, and J. Rathsman, *Comput. Phys. Commun.* **101**, 108 (1997).
- [34] Sjöstrand, Torbjorn, *Comput. Phys. Commun.* **39**, 347 (1986).
- [35] Akushevich, I. and Böttcher, H. and Ryckbosch, D., (1998), [hep-ph/9906408](https://arxiv.org/abs/hep-ph/9906408).
- [36] R. Brun, R. Hagelberg, M. Hansroul, and J. C. Lassalle, CERN-DD-78-2-REV.
- [37] F. Ravndal, *Phys. Lett.* **B43**, 301 (1973).
- [38] R. Kingsley, *Phys. Rev.* **D10**, 1580 (1974).
- [39] R. N. Cahn, *Phys. Lett.* **B78**, 269 (1978).
- [40] R. N. Cahn and J. D. Jackson, *Phys. Rev.* **D42**, 3690 (1990).
- [41] D. Boer and P. J. Mulders, *Phys. Rev.* **D57**, 5780 (1998).
- [42] D. Boer and P. J. Mulders, *Nucl. Phys.* **B569**, 505 (2000).
- [43] F. Giordano and R. Lamb, *AIP Conf. Proc.* **1149**, 423 (2009).
- [44] J. G. Rubin, *Ph.D. thesis*, University of Illinois at Urbana-Champaign (2009), DESY-THESIS-2009-045.
- [45] J. Pumplin *et al.*, *JHEP* **0207**, 012 (2002).
- [46] J. Pumplin *et al.*, *JHEP* **0602**, 032 (2006).
- [47] Sjöstrand, Torbjorn, *Comput. Phys. Commun.* **82**, 74 (1994).
- [48] A. Airapetian *et al.* (HERMES Collaboration), HERMES multiplicity database, <http://www-hermes.desy.de/multiplicities/>; mail-to: management@hermes.desy.de; and Durham HEP database, <http://durpdg.dur.ac.uk>.